Title: Tropical cyclone risk to global electricity supply

Authors:
Fred Thomas[1], Yu Mo[1], Jianan Rui[2], Tom Russell[1], Max Robertson[1], Jasper Verschuur[3], Raghav Pant[1], and Jim W Hall[1]

Affiliations:
[1]Environmental Change Institute, University of Oxford
[2]Department of Statistics, University of Chicago
[3]Faculty of Technology, Policy and Management, Delft University of Technology

This paper was submitted to Nature Energy 28th June 2024. As of 11th September 2025, this paper is under review with Nature Energy -- it has not yet been published.

Tropical cyclone risk to global electricity supply

Fred Thomas[1], Yu Mo[1], Jianan Rui[2], Tom Russell[1], Max Robertson[1], Jasper Verschuur[3], Raghav Pant[1], and Jim W Hall[1]

[1]Environmental Change Institute, University of Oxford
[2]Department of Statistics, University of Chicago
[3]Faculty of Technology, Policy and Management, Delft University of Technology

September 11, 2025

Abstract

To analyse the risks from Tropical Cyclones (TC) to electricity supply, we have combined a large ensemble of TC simulations with a spatial model of power networks and people served, for the entire TC belt globally. The model of electricity power failure, measured in terms of population disrupted, was calibrated against nighttime lights satellite imagery of historic TC events. Use of spatially coherent TC simulations enabled the calculation of electricity supply losses at national, regional and global scales for a range of return periods. We estimate that between 65 and 80 million people lose electric power with a return period of 1 in 100 years, depending on the TC model. Most regions show a worsening of TC-induced outages under climate change (RCP8.5 2050), except for the North Indian Ocean, where there is disagreement between TC models. Climate model uncertainty (across four GCMs) influences the estimated global population at risk by a factor of 0.91-1.05 in 2050.

Electricity supplies are essential for people and economies [1]. Tropical cyclones (TCs) can be extremely disruptive to electricity networks, with strong winds, intense precipitation and storm surges damaging supply, transmission and distribution infrastructure. Nine out of ten of the largest blackouts in the US have been caused by TCs and three of the largest ever recorded blackout events worldwide were also caused by TCs [2]. Typhoon Haiyan, the most significant of these, struck the Philippines in 2013 and caused approximately $10 billion in damages to assets, or 3.7% of Phillipine GDP [3], disrupting an estimated 6.1 billion customer-hours of electricity supply [4]. Since 2000, approximately $60 billion a year in short-term economic losses globally have been caused by TCs [5]. Additionally, evidence suggests that TC events have a negative impact on national income, relative to a pre-event trend, for many years [6].

The risks of power failure caused by TCs can be mitigated by enhancing system resilience, for instance by improving the resistance of assets to extreme winds (e.g. by upgrading to steel/concrete distribution poles or burying transmission cables), by reducing the number of people affected (e.g. back-up supply capacity and/or redundancy in the transmission/distribution network), or by speeding up the restoration of services (e.g. emergency planning and adequate resourcing of repair crews) [7]. Prioritizing these interventions to enhance resilience should be informed by quantified risk analysis, as the benefit of any intervention is calculated as the difference between the risk of failure (combining probability and consequences) with and without the intervention.

Asset-level risk assessment for power systems is well established, including larger scales (country or regional) [8]. However, system-scale assessments covering multiple countries are much more challenging, because the extent of system failure is sensitive to the spatial extent of the TC, the spatial configuration of the electric power system, and differences in failure thresholds of assets [9][10]. In addition, proper characterisation of low probability-high consequence events (i.e. 'tail risk') requires analysis of the spatial evolution of a very large number of plausible extreme TC events.

Previous studies have either simulated failures in power flow models based on national electricity network data or have used more realistic spatial representations of TC events combined with statistical predictions of the impacts of power outages (e.g. [11], [12]) for the east coast of the USA). However, commonly adopted power flow model studies are challenging to scale-up to examine large numbers of simulated events over very large domains with scarce system data, whilst statistical methods lack an adequate representation of the electricity network, and therefore the ability of the electricity system to buffer certain network failures. Yet, there is a growing need to scale-up power

flow simulations. For instance, publicly listed energy utilities are increasingly required to report on the physical climate risks to which they are exposed, whilst energy regulators are adopting risk-based approaches to network reliability reporting, which seek to stress-test possible events that are more severe than past observations.

Here, we bridge between these two approaches by constructing reduced-complexity wide-scale electricity network models, which can simulate the electricity supply from generation sites to electricity users. We have used historic (IBTrACS [13]) and synthetic (STORM [14] & IRIS[15]) storm track models representing observed climate and future (mid-century under RCP 8.5) storm events, downscaled with a parametric wind model (see Methods). We have built connected electricity supply and transmissions models for approximately 100 cyclone-prone countries, connected to spatially mapped population. To enable comparison, we do not change the population maps in the future scenarios. The sensitivity of electricity assets to TC winds is calibrated with VIIRS night time lights satellite imagery (see Methods). We used this combination of models to quantify the risk of electricity outages at present and in the future.

Results

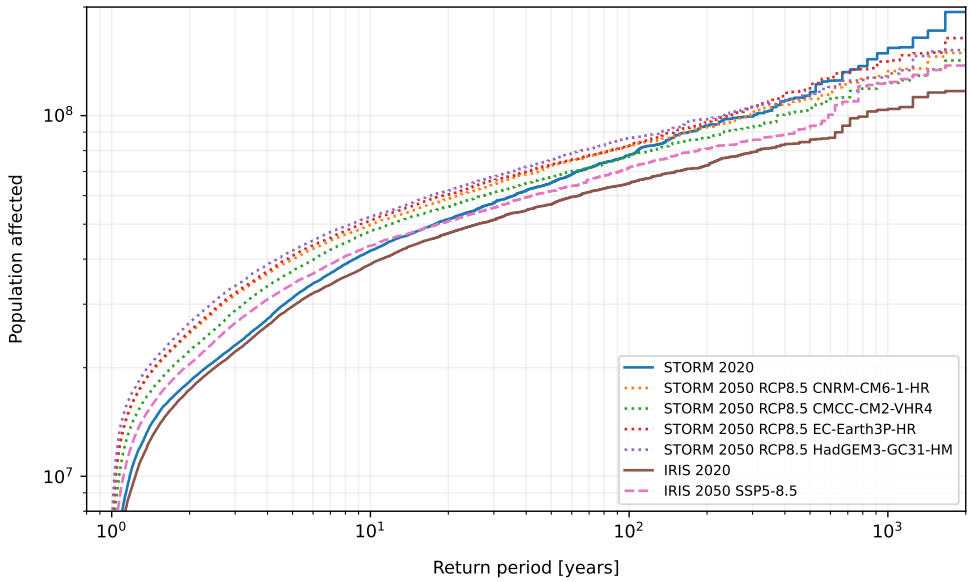

Figure 1: Global population affected by electric power disruptions due to TC events as a function of return period for both TC models in the present and future climate (2050 RCP8.5).

To estimate the global disruption, for every storm we sum the population that is dependent on the failed power network assets. We then select the largest storm in each year and sort them in ascending order. In this way we estimate that for the present day, the 0.01 annual exceedance probability (1 in 100 year return period) disruption from TCs is between 65 million (IRIS) and 80 million (STORM) people (Figure 1). For IRIS, 100-year return period disruption under RCP8.5 in 2050 is projected to be approximately 10% larger than in the present day. For STORM, future changes at return periods below 100 years yield increases in risk, but for lower probability events, the present day shows worse outcomes than in 2050 under RCP8.5. This is due to a projected decrease in Category 5 storms in the Bay of Bengal, as storm genesis locations move northward and cyclones do not have as much time to intensify before making landfall in populous north-east India and Bangladesh [16].

Figure 2 shows the population affected in a 50-year return period TC for selected countries. This is based on country calibration of power network vulnerability where available and country-income level calibration if no per-country calibration is available (see Supplementary Information).

We calculate the Expected Annual Population Affected (EAPA) on local administrative regions (a global composite of admin levels 0, 1 and 2, using the highest resolution available for each nation state) (Figure 3). To provide a measure that is more easily comparable across space, we normalize this EAPA by the connected population in the region. Our results reflect the areas most prone to

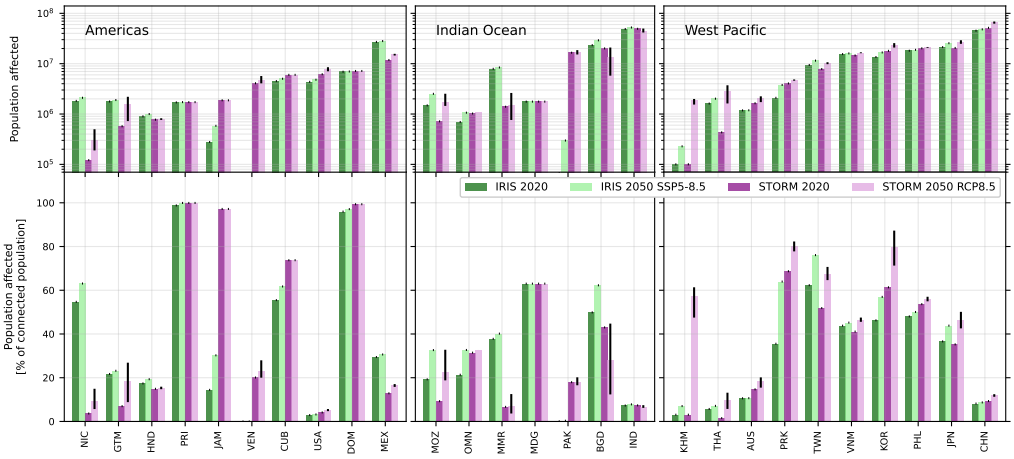

Figure 2: 1 in 50 year population affected in the present day and RCP8.5 in 2050 from STORM and IRIS TC models. The upper panel gives an absolute population affected at this return period; the lower panel gives that number as the percentage of the connected population. Error bars are present for the STORM RCP8.5 2050 scenario, showing the range of results from the various GCMs. The future IRIS scenario uses a multi-GCM mean as input and is therefore single valued.

damage from TCs: the North and South Indian Ocean, the East, South and West Pacific, and the North Atlantic basins. The maximum EAPA per connected person in either STORM or IRIS for the present day is ≈ 0.171 and is for the municipality of Santa Praxedes, at the northern tip of the Philippines.

The greatest difference between observed TCs (IBTrACS) and the contemporary synthetic sets (STORM & IRIS) is to be found in the North Indian Ocean, where the historical record is limited. Here, the maximum historic wind speed found in our cleaned IBTrACS set is 68ms^{-1}, whereas for both contemporary STORM and IRIS, the maximum is 95ms^{-1}. That is, the synthetic sets contain tail events which significantly exceed the severity of storms witnessed in the near past.

All of the results show estimates of population affected for the historic (2020) baseline event set and for the version of the event set conditioned on 2050 climate conditions. Whilst IRIS is based on a multi-model mean of General Circulation Models (GCMs), and so individual GCM results cannot be obtained, the STORM model tracks are available for a variety of GCMs. We note that generally there are substantial differences between results from the STORM and IRIS synthetic tropical cyclone models.

This is mostly borne out in our results, where comparing present-day (2020 epoch) with RCP8.5 in the 2050 epoch shows increases in expected disruption across the world. For example, in Figure 2 in the West Pacific, every country is projected to experience an increase in the magnitude of disruption under future conditions. The Korean peninsula, Taiwan and Japan all show substantial increases in the fraction of population at risk in the future. For the Americas, similar results are found, with substantial percentage increases for Cuba, Jamaica and Mexico. The pictured 1 in 50 year contemporary TC events already overwhelm the power networks of Puerto Rico and the Dominican Republic, but these countries are also predicted to experience an increased risk in the future scenario. In the case of the Indian Ocean, countries in the south, like Mozambique and Madagascar, are predicted to experience an increased risk. In the north, Oman shows a growth in risk for IRIS and a highly uncertain growth for STORM. IRIS indicates minimal risk to southern Pakistan currently or in the future, with the STORM model projecting more of an impact. Moving from the Arabian Sea to the Bay of Bengal, Bangladesh, India and Myanmar all see future increases in risk under IRIS, in the case of Bangladesh substantially so. STORM estimates future cyclone activity in the area to decrease and so we see a reduction in risk for Bangladesh and India.

Future scenarios are displayed as maps of percentage change in EAPA per connected person in Figure 4. In the most highly impacted municipality of Santa Praxedes, at the northern tip of the Philippines under RCP8.5, the maximum EAPA per connected person for STORM 2050 is 0.246 (44% increase on the present day value of 0.171) and for IRIS 2050 is 0.196 (15% increase). These inter-model differences are often greater in magnitude than inter-scenario differences within a given model. For example, for IRIS a 1 in 50 year disruption event impacting Jamaica affects 15%-29% (contemporary and RCP8.5 2050, respectively) of the population, whereas with STORM, the grid

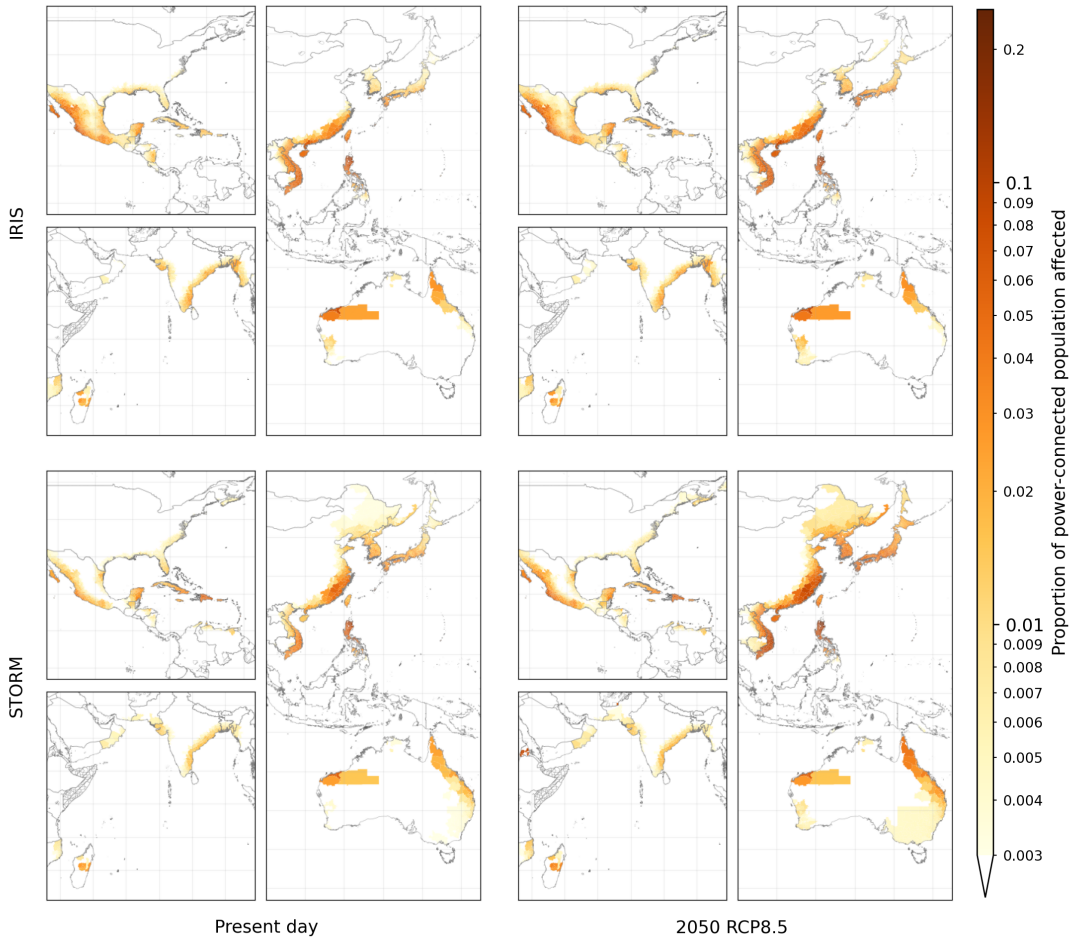

Figure 3: Expected annual population affected per connected person in local administrative units. The upper panels are IRIS TC model; lower panels are STORM TC model. The left panels are for the present day, 2020; right hand panels are under RCP8.5 in 2050. A value of 1 would mean each grid connected person in the given area is expected to experience TC wind induced disruption every year, on average.

is completely overwhelmed under either scenario.

The variation in results between different GCMs can be substantial. We see greater disruption caused by TCs from 'hot models', i.e. those with an Equilibrium Climate Sensitivity (ECS) in excess of 4K, such as HadGEM3-GC3.1, EC-Earth3P-HR or CNRM-CM6-1-HR than by those in the medium ECS range, 2.87K $<$ ECS $<$ 4K, such as CMCC-CM2-VHR4 (see Figure 5). Note that models with a higher ECS tend to exceed the mean, with the lowest ECS GCM, CMCC-CM2-VHR4, tending under the multi-GCM mean. The narrowed GCM spread for higher return periods is expected as more significant events are more likely to saturate a country's grid, leading to the same projection for number of people disrupted, regardless of GCM. Unfortunately STORM does not include a GCM with a low ($<$ 2.87K) ECS.

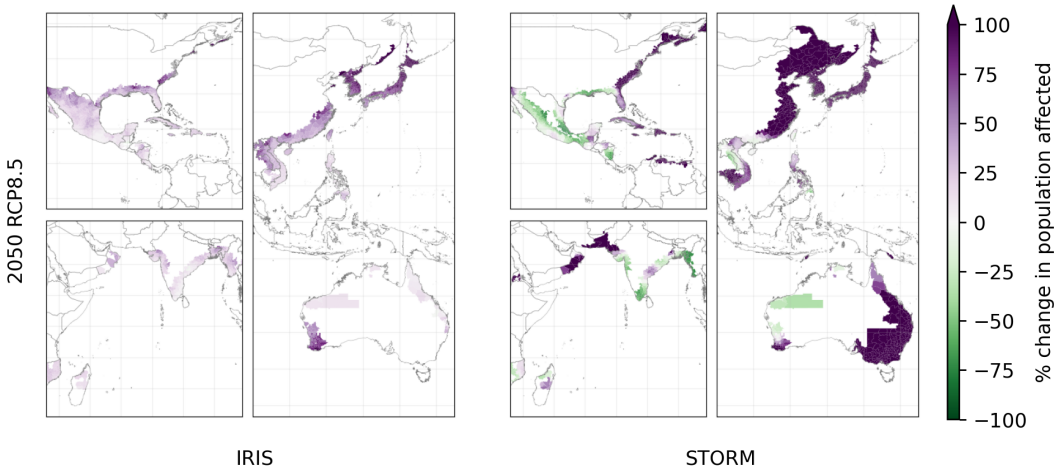

Figure 4: Percentage change in expected annual population affected per connected person in local administrative units. The change is given relative to the present day (2020 climate) for both the IRIS and STORM TC models. Areas with an EAPA per connected person below the minimum threshold shown in Figure 3 are masked out.

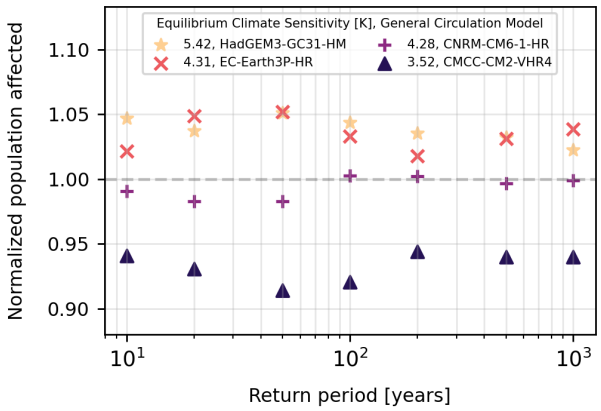

Figure 5: Population affected for the four STORM GCMs. Ordinate values are global means of per-country people affected values normalized by the multi-GCM mean for that country and return period. The Equilibrium Climate Sensitivity (ECS) is given for each GCM, although not all values were available, in which case we used an ECS from a GCM of the same model family.

Discussion and conclusions

Electricity outages due to climate extremes are extremely disruptive for society. As such, there is an increasing need to quantify physical climate risks to power networks to inform network planning, investment, design and asset management. However, hitherto, large-scale climate risk analysis of power networks has been challenging because of the need to simulate several thousands of plausible climate extremes and their resulting impacts. In this study, we have developed a reduced complexity power flow model that explicitly captures the geospatial location of electricity infrastructure, and can also simulate the spatial rerouting of electricity supplies during and after disruptions. This model, which is calibrated on historical events, is stress-tested with thousands of plausible cyclone wind fields, allowing us to quantify the likelihood and impacts of power outages globally. Our modelling results allow decision-makers to understand at what probability of occurrence, the networks reaches a state of intolerable outages.

Our results indicate that electricity networks of a smaller spatial size show greater vulnerability to TC risk. For example, for the 1-in-50 year disruption event, the Dominican Republic's grid is overwhelmed and a projected 100% of the population are at risk of losing power. For the

neighbouring but larger island of Cuba, the figure is 60-70% depending on scenario. In other words, smaller grids have less redundancy against tail risk events, requiring alternative ways to buffer the impacts of extreme cyclonic events, such as additional asset strengthening and/or local back-up generation.

At present, we estimate the expected annual population affected to be 54-57 million per year, with hotspots in the populated, cyclone-prone, regions in China, India, the Caribbean and Mexico. Due to climate change alone, this number could increase by 30-68% in 2050, depending on the synthetic storm dataset adopted. For many countries, the uncertainty of future cyclone risk across the climate models is equal in size, or even larger, than the net climate signal and differences between models, indicating that the model results are sensitive to model and climate uncertainties. Hence, we advocate for more work comparing the various available TC models, their strengths and their weaknesses, along the lines of, for example, Meiler et al. [17].

The resistance of electricity assets to extreme wind speeds (i.e. the failure threshold, which is a crucial calibrated parameter in our framework) is not uniform across regions, but often assumed to be because of data limitations [18]. In this analysis we have specified this wind sensitivity with a failure threshold, by analysing over 300 historical TC outage events using night-time light satellite observations. We find notable differences across regions, with higher thresholds in the USA, Philippines and Japan, and lower thresholds in Mexico and India. However, we also found that identifying a generic region-specific threshold was difficult, underlining the need to improve our understanding of the regional reliability of electricity systems, such as design guidelines, materials properties, and other engineering standards. Moreover, we acknowledge that our failure identification method uses a simple wind speed threshold, which is a simplification of real world asset failure. Instead, a better representation would also include other variables (e.g. precipitation and coastal storm surges) and model the conditional probability of failure given the hazard variables (a fragility curve), which would significantly increase computational resources to execute the risk analysis. For tractability's sake, we take the threshold wind speed approach as a simplifying assumption.

We note the ongoing discussion about how to best interpret results from CMIP6 models [19], with the IPCC choosing to down-weight models outside of the likely ECS range [20] but others arguing that the earth system's ECS is indeed closer to that implied by the hot models [21]. As the wide uncertainty range on ECS has hardly narrowed over 40 years, we advocate for including hot model results as an important worst case.

A paucity of quality historical data also hampers the degree to which we can draw conclusions about the effects of recent warming on TC attributes. However, it has been theorized for some time that warmer climates would lead to an increase in maximum attainable TC intensity, mostly due to increases in ocean surface temperature providing a greater energy source for storms to draw upon [22]. Future projections using high-resolution dynamic models predict average TC intensity increasing by 2-11% by 2100, with total TC frequency falling by 3-34% [23].

Despite the aforementioned limitations, we believe our modelling framework has value in terms of performing climate stress-testing exercises on very large scale, in particular when there is a need to screen climate risks across many assets and regions. Assessments, such as those presented here are relevant to assess investor and insurance exposure to spatially dependent climatic extremes. In addition, it can serve as an initial screening to identify critical elements within national electricity systems, to allocate scarce resources to improve the robustness of the at-risk assets, as well as quantifying the adaptation needs of electricity systems as whole.

Methods

Our analysis integrates (Figure 6): (a) a geospatial electricity transmission and distribution network model and (b) routing of electricity supply to demand in the network. (c) The characteristics of observed TCs are downscaled and (d) intersected with the electricity network. In step (e) the network asset failure threshold is calibrated to maximise the match of the failed areas with night time light data. The set of historic and future storm events is then run over the calibrated model to estimate the statistics of disruption at different return periods. The model is publicly available [24] as part of an open source snakemake [25] workflow.

Wind footprints

TCs are cyclonic events that originate in the tropics and propagate in a north-westerly direction in the Northern Hemisphere and south-westerly in the Southern Hemisphere. They are widely

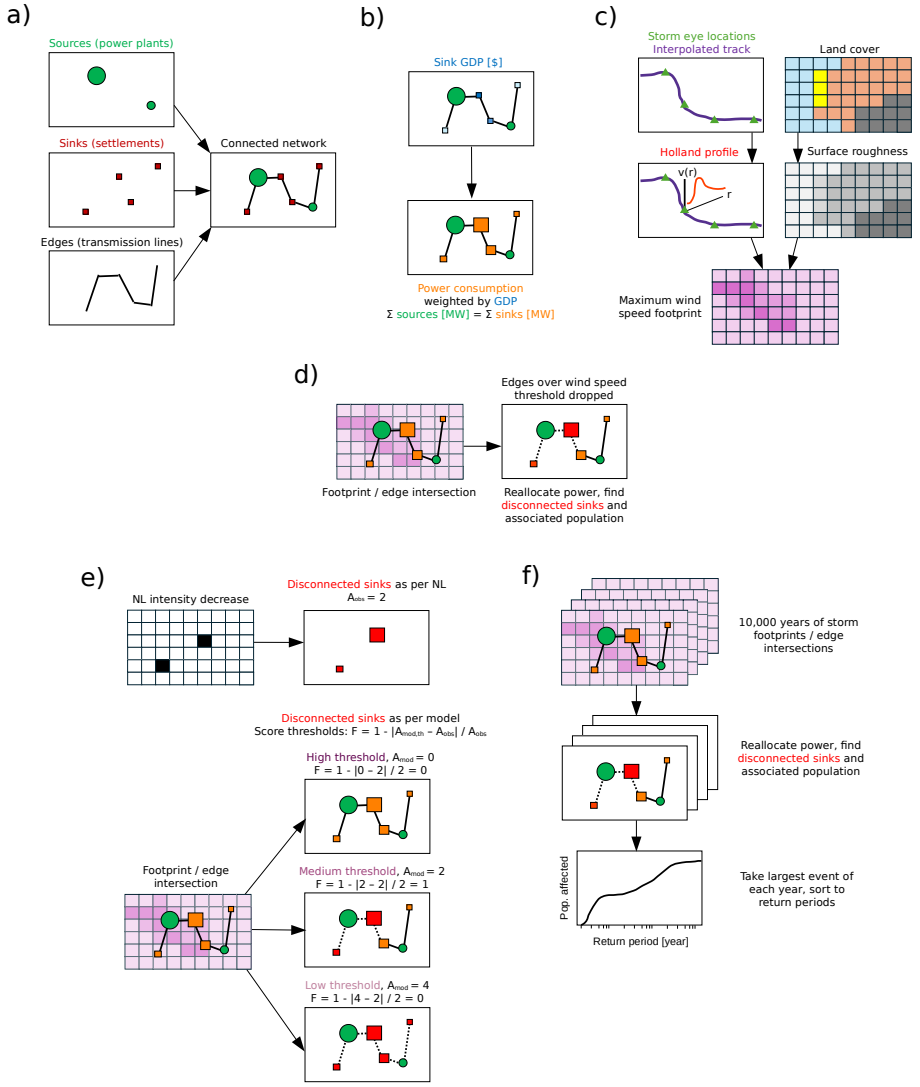

Figure 6: Schematic diagram of study method, broken down into a) Electricity network generation, b) Allocation of generation capacity from power plants to consuming areas, c) Wind speed footprint generation, d) Footprint/network intersection, e) Damage threshold calibration from night time lights (NL) and f) Event set simulation.

studied and modelled [26][27][28][29][30], and the wind field can be characterized with a track and a small number of parameters for each track point.

To explore the risk to electric power networks, we require a maximum wind speed field (wind footprint) for each storm event. STORM [14] and IRIS [15]) are stochastic TC models for generating synthetic events. In both cases, the synthetic track data is generated by fitting distributions to historic data of TC genesis location, minimum pressure, wind speed, among others, and then sampling from these distributions to create new storm tracks. Similarly, storms are propagated by sampling from historic distributions of longitude and latitude change. STORM and IRIS are both available for present day (2020) and 2050 under RCP8.5/SSP5-8.5. We note that RCP8.5 is an unlikely scenario, however, at mid-century the warming differences between RCPs are minimal.

There are some differences between the TC track models. IRIS does not include the track intensification phase, i.e. it only reports track attributes after storms have reached their Lifetime Maximum Intensity (LMI). Whilst IRIS uses the model mean of many General Circulation Models (GCMs) as input, STORM is available per-GCM, allowing an exploration of inter-GCM variability.

As per Figure 6 (c), downscaling from storm tracks to wind fields starts from a storm track, with regular records of storm eye position, minimum pressure, maximum wind speed and radius to maximum wind speed. A Holland wind model [31] is used to estimate the axisymmetric rotational wind vectors across the domain, as a function of distance from the storm eye (see Supplementary

Information).

The surface level winds experienced by built infrastructure are moderated by the complex dynamics of the planetary boundary layer, where moving air is significantly influenced by the friction of the earth's surface [32]. We account for this by downscaling the parametric winds by reduction factor as in [30] (see Supplementary Information).

Electricity network

The electricity networks used in this study are comprised of nodes, which are either sources (electricity generators) or sinks (electricity consuming settlements), and edges, which are electricity transmission/distribution lines. Sources and their nominal capacities are drawn from the World Resources Institute global power plant database [33]. Sinks are from Gridfinder [34], where VIIRS night time lights (NTL) satellite imagery was processed to estimate where electrified (and by assumption, grid connected) settlements exist. These sinks are polygonised and annotated with their encompassing population [35] and GDP value [36] as per Figure 6 a) and b).

Network edges were also taken from the Gridfinder dataset. Gridfinder mainly derived the high-voltage transmission network from OpenStreetMap [37], with lower voltage distribution lines algorithmically generated by a shortest path routing from high-voltage lines, along roads, to settlements.

We build connected electricity networks for around 100 countries, where a country is an entry in the GADM3.6 administrative boundaries database [38]. It is the case that some existing electricity grids are connected across borders. These interconnections may improve network resilience, given the ability of neighbour's unused generating capacity to meet disrupted demand. However, in this study no interconnections between countries are considered to a) reduce model complexity and b) as levels of inter-country grid connection are low in the TC belt[1].

For each country network, powerplants are connected to their nearest edge, similarly for electricity consuming settlements. Most country networks derived from the Gridfinder data have more than one network component. This is often due transmission lines that exist in reality but are absent from the Gridfinder data[2]. Each country typically has one giant component containing the majority of the edges and nodes, with some smaller components comprising the remainder.

Available power generating capacity for a given network component is allocated from the power generating nodes to the consuming settlement nodes, weighted by consuming nodes' respective GDP[3]. This allocation is not constrained by engineering considerations such as maximum power flow per line. More detailed grid data would be necessary for such an allocation.

Outage model

Transmission and distribution lines which experience a wind speed in excess of a threshold, v_{th}, are removed from the network as per Figure 6 (d). Power from still connected generators is reallocated across the new network topology. In this way, per event, we can quantify the number of people that lose electric power during TC events, taking the ability of the system to redistribute supply during and after disruptions into account. This is repeated across many storms, as per Figure 6 (f), to explore return periods and tail risk.

The outage model was calibrated and validated with VIIRS night time light observations was from 252 and 63 storms respectively, as described in the Supplementary Information.

References

[1] Falk, J., Angelmahr, M., Schade, W. & Schenk-Mathes, H. Socio-economic impacts and challenges associated with the electrification of a remote area in rural Tanzania through a mini-grid system. *Energy, Ecology and Environment* **6**, 513–530 (2021). URL https://link.springer.com/10.1007/s40974-021-00216-3.

[2] Lin, N. Tropical cyclones and heatwaves. *Nature Climate Change* **9**, 579–580 (2019). URL https://www.nature.com/articles/s41558-019-0537-2.

[1] Although future plans for the ASEAN Power Grid [39] may change this.

[2] A more comprehensively connected global electricity grid dataset would be very valuable for these kinds of analysis.

[3] As the GDP data employed is almost always single-valued for a given country, this often reduces to a weighting by population.

[3] Santos, C. T., Toda, L., Orduña, J. R., Santos, F. D. & Ferrão, J. The impacts of Typhoon Haiyan in the Philippines: Implications to land use planning. *Climate, Disaster and Development Journal* **1**, 57–66 (2015). URL http://www.cddjournal.org/article/view/vol01-iss01-006.

[4] Houser, Trevor & Marsters, Peter. The World's Second Largest Blackout (2018). URL https://rhg.com/research/puerto-rico-hurricane-maria-worlds-second-largest-blackout/.

[5] Delforge, D. *et al.* EM-DAT: the Emergency Events Database (2023). URL https://www.researchsquare.com/article/rs-3807553/v1.

[6] Hsiang, S. & Jina, A. The Causal Effect of Environmental Catastrophe on Long-Run Economic Growth: Evidence From 6,700 Cyclones. Tech. Rep. w20352, National Bureau of Economic Research, Cambridge, MA (2014). URL http://www.nber.org/papers/w20352.pdf.

[7] Ji, C. *et al.* Large-scale data analysis of power grid resilience across multiple US service regions. *Nature Energy* **1**, 16052 (2016). URL https://www.nature.com/articles/nenergy201652.

[8] Ye, M., Koks, E., Ward, P., Bloemendaal, N. & Nirandjan, S. Risk analysis of natural hazards to power grids in Southeast and East Asia. vol. EGU23-895 (Vienna, 2023).

[9] Ahmed, A., Arthur, C. & Edwards, M. Collapse and pull – down analysis of high voltage electricity transmission towers subjected to cyclonic wind. *IOP Conference Series: Materials Science and Engineering* **10**, 012004 (2010). URL https://iopscience.iop.org/article/10.1088/1757-899X/10/1/012004.

[10] Jamieson, M. R., Strbac, G. & Bell, K. R. Quantification and visualisation of extreme wind effects on transmission network outage probability and wind generation output. *IET Smart Grid* **3**, 112–122 (2020). URL https://onlinelibrary.wiley.com/doi/10.1049/iet-stg.2019.0145.

[11] Alemazkoor, N. *et al.* Hurricane-induced power outage risk under climate change is primarily driven by the uncertainty in projections of future hurricane frequency. *Scientific Reports* **10**, 15270 (2020). URL https://www.nature.com/articles/s41598-020-72207-z.

[12] Guikema, S. D. *et al.* Predicting hurricane power outages to support storm response planning. *Ieee Access* **2**, 1364–1373 (2014).

[13] Kruk, M. C., Knapp, K. R. & Levinson, D. H. A Technique for Combining Global Tropical Cyclone Best Track Data. *Journal of Atmospheric and Oceanic Technology* **27**, 680–692 (2010). URL http://journals.ametsoc.org/doi/10.1175/2009JTECHA1267.1.

[14] Bloemendaal, N. *et al.* Generation of a global synthetic tropical cyclone hazard dataset using STORM. *Scientific Data* **7**, 40 (2020). URL https://www.nature.com/articles/s41597-020-0381-2.

[15] Sparks, N. & Toumi, R. The Imperial College Storm Model (IRIS) Dataset. *Scientific Data* **11**, 424 (2024). URL https://www.nature.com/articles/s41597-024-03250-y.

[16] Bloemendaal, N. *et al.* A globally consistent local-scale assessment of future tropical cyclone risk. *Science Advances* **8**, eabm8438 (2022). URL https://www.science.org/doi/10.1126/sciadv.abm8438. Publisher: American Association for the Advancement of Science.

[17] Meiler, S. *et al.* Intercomparison of regional loss estimates from global synthetic tropical cyclone models. *Nature Communications* **13**, 6156 (2022). URL https://www.nature.com/articles/s41467-022-33918-1.

[18] Verschuur, J. *et al.* Quantifying climate risks to infrastructure systems: A comparative review of developments across infrastructure sectors. *PLoS Climate* **3**, e0000331 (2024).

[19] Hausfather, Z., Marvel, K., Schmidt, G. A., Nielsen-Gammon, J. W. & Zelinka, M. Climate simulations: recognize the 'hot model' problem. *Nature* **605**, 26–29 (2022). URL https://www.nature.com/articles/d41586-022-01192-2.

[20] Sherwood, S. C. *et al.* An Assessment of Earth's Climate Sensitivity Using Multiple Lines of Evidence. *Reviews of Geophysics* **58**, e2019RG000678 (2020). URL https://agupubs.onlinelibrary.wiley.com/doi/10.1029/2019RG000678.

[21] Hansen, J. E. *et al.* Global warming in the pipeline. *Oxford Open Climate Change* **3**, kgad008 (2023). URL https://academic.oup.com/oocc/article/doi/10.1093/oxfclm/kgad008/7335889.

[22] Emanuel, K. A. The dependence of hurricane intensity on climate. *Nature* **326**, 483–485 (1987).

[23] Knutson, T. R. *et al.* Tropical cyclones and climate change. *Nature Geoscience* **3**, 157–163 (2010). URL https://www.nature.com/articles/ngeo779.

[24] Thomas, F., Russell, T., Lestang, T., Robertson, M. & Jaquiery, M. Open-data Global Infrastructure Risk/Resilience Analysis (2023). URL https://doi.org/10.5281/zenodo.8321432.

[25] Mölder, F. *et al.* Sustainable data analysis with Snakemake. *F1000Research* **10**, 33 (2021). URL https://f1000research.com/articles/10-33/v1.

[26] Tan, C. & Fang, W. Mapping the Wind Hazard of Global Tropical Cyclones with Parametric Wind Field Models by Considering the Effects of Local Factors. *International Journal of Disaster Risk Science* **9**, 86–99 (2018). URL http://link.springer.com/10.1007/s13753-018-0161-1.

[27] Willoughby, H. E. & Rahn, M. E. Parametric Representation of the Primary Hurricane Vortex. Part I: Observations and Evaluation of the Holland (1980) Model. *Monthly Weather Review* **132**, 3033–3048 (2004). URL http://journals.ametsoc.org/doi/10.1175/MWR2831.1.

[28] Powell, M. D., Uhlhorn, E. W. & Kepert, J. D. Estimating Maximum Surface Winds from Hurricane Reconnaissance Measurements. *Weather and Forecasting* **24**, 868–883 (2009). URL https://journals.ametsoc.org/doi/10.1175/2008WAF2007087.1.

[29] Holland, G. J., Belanger, J. I. & Fritz, A. A Revised Model for Radial Profiles of Hurricane Winds. *Monthly Weather Review* **138**, 4393–4401 (2010). URL http://journals.ametsoc.org/doi/10.1175/2010MWR3317.1.

[30] Lin, N. & Chavas, D. On hurricane parametric wind and applications in storm surge modeling: HURRICANE WIND AND SURGE MODELING. *Journal of Geophysical Research: Atmospheres* **117**, n/a–n/a (2012). URL http://doi.wiley.com/10.1029/2011JD017126.

[31] Holland, G. J. An Analytic Model of the Wind and Pressure Profiles in Hurricanes. *Monthly Weather Review* **108**, 1212–1218 (1980). URL http://journals.ametsoc.org/doi/10.1175/1520-0493(1980)108<1212:AAMOTW>2.0.CO;2.

[32] Done, J. M. *et al.* Modelling global tropical cyclone wind footprints. *Natural Hazards and Earth System Sciences* **20**, 567–580 (2020). URL https://nhess.copernicus.org/articles/20/567/2020/.

[33] Global Energy Observatory, Google, KTH Royal Institute of Technology in Stockholm, Enipedia & World Resources Institute. Global Power Plant Database (2021). URL https://datasets.wri.org/dataset/globalpowerplantdatabase.

[34] Arderne, C., Zorn, C., Nicolas, C. & Koks, E. E. Predictive mapping of the global power system using open data. *Scientific Data* **7**, 19 (2020). URL https://www.nature.com/articles/s41597-019-0347-4. Number: 1 Publisher: Nature Publishing Group.

[35] SM, C. F., K, M., M, P., E, D.-W. & J, M. *Development of new open and free multi-temporal global population grids at 250 m resolution* (AGILE, 2016). URL https://agile-online.org/Conference_Paper/cds/agile_2016/shortpapers/152_Paper_in_PDF.pdf.

[36] Kummu, M., Taka, M. & Guillaume, J. H. A. Gridded global datasets for Gross Domestic Product and Human Development Index over 1990–2015. *Scientific Data* **5**, 180004 (2018). URL https://www.nature.com/articles/sdata20184.

[37] OpenStreetMap contributors. OpenStreetMap (2023). URL https://www.openstreetmap.org/. Published: https://www.openstreetmap.org.

[38] University of California, Berkeley. Global Administrative Areas (2018). URL http://www.gadm.org/.

[39] ASEAN. ASEAN Power Grid (2015). URL https://asean.org/wp-content/uploads/images/2015/October/outreach-document/Edited%20APG-3.pdf.

[40] Sun, Z., Zhang, B., Zhang, J. A. & Perrie, W. Examination of Surface Wind Asymmetry in Tropical Cyclones over the Northwest Pacific Ocean Using SMAP Observations. *Remote Sensing* **11**, 2604 (2019). URL https://www.mdpi.com/2072-4292/11/22/2604.

[41] Arino, O. *et al.* Global Land Cover Map for 2009 (GlobCover 2009) (2009).

[42] Davis, N. N. *et al.* The Global Wind Atlas: A High-Resolution Dataset of Climatologies and Associated Web-Based Application. *Bulletin of the American Meteorological Society* **104**, E1507–E1525 (2023). URL https://journals.ametsoc.org/view/journals/bams/104/8/BAMS-D-21-0075.1.xml.

[43] Kepert, J. & Wang, Y. The Dynamics of Boundary Layer Jets within the Tropical Cyclone Core. Part II: Nonlinear Enhancement. *Journal of the Atmospheric Sciences* **58**, 2485–2501 (2001). URL http://journals.ametsoc.org/doi/10.1175/1520-0469(2001)058<2485:TDOBLJ>2.0.CO;2.

[44] ORNL DAAC. MODIS and VIIRS Land Products Global Subsetting and Visualization Tool (2023). URL https://daac.ornl.gov/cgi-bin/dsviewer.pl?ds_id=1379.

[45] Aronica, G., Bates, P. D. & Horritt, M. S. Assessing the uncertainty in distributed model predictions using observed binary pattern information within GLUE. *Hydrological Processes* **16**, 2001–2016 (2002). URL https://onlinelibrary.wiley.com/doi/10.1002/hyp.398.

[46] Montoya-Rincon, J. P. *et al.* On the use of satellite nightlights for power outages prediction. *IEEE Access* **10**, 16729–16739 (2022).

[47] Román, M. O. *et al.* Satellite-based assessment of electricity restoration efforts in puerto rico after hurricane maria. *PloS one* **14**, e0218883 (2019).

[48] Shah, Z., Carvallo, J. P., Hsu, F.-C. & Taneja, J. The inequitable distribution of power interruptions during the 2021 texas winter storm uri. *Environmental Research: Infrastructure and Sustainability* **3**, 025011 (2023).

[49] Wang, Z. *et al.* Monitoring disaster-related power outages using nasa black marble nighttime light product. *The International Archives of the Photogrammetry, Remote Sensing and Spatial Information Sciences* **42**, 1853–1856 (2018).

[50] Chen, M., Hu, Y., Cao, X., Li, S. & Liu, L. Assessing electricity supply reliability by detection of anomalies in daily nighttime light. *IEEE Journal of Selected Topics in Applied Earth Observations and Remote Sensing* (2024).

[51] Mitsova, D. *et al.* Using nighttime light data to explore the extent of power outages in the florida panhandle after 2018 hurricane michael. *Remote Sensing* **16**, 2588 (2024).

[52] Hu, Y., Zhou, X., Yamazaki, D. & Chen, J. A self-adjusting method to generate daily consistent nighttime light data for the detection of short-term rapid human activities. *Remote Sensing of Environment* **304**, 114077 (2024).

[53] Wang, Z. *et al.* Quantifying uncertainties in nighttime light retrievals from suomi-npp and noaa-20 viirs day/night band data. *Remote Sensing of Environment* **263**, 112557 (2021).

[54] Tan, X., Zhu, X., Chen, J. & Chen, R. Modeling the direction and magnitude of angular effects in nighttime light remote sensing. *Remote Sensing of Environment* **269**, 112834 (2022).

[55] Li, T. *et al.* Continuous monitoring of nighttime light changes based on daily nasa's black marble product suite. *Remote Sensing of Environment* **282**, 113269 (2022).

[56] Román, M. O. & Stokes, E. C. Holidays in lights: Tracking cultural patterns in demand for energy services. *Earth's future* **3**, 182–205 (2015).

[57] Zhao, X. *et al.* Npp-viirs dnb daily data in natural disaster assessment: Evidence from selected case studies. *Remote Sensing* **10**, 1526 (2018).

[58] Zheng, Q., Weng, Q., Zhou, Y. & Dong, B. Impact of temporal compositing on nighttime light data and its applications. *Remote Sensing of Environment* **274**, 113016 (2022).

[59] Bluefire Studios LLC. PowerOutage.Us (2021). URL https://poweroutage.us/. Published: https://poweroutage.us/.

Supplementary Information

Holland wind model

A Holland wind model [31] is used to estimate the axisymmetric rotational wind vectors across the domain, as a function of distance from the storm eye.

$$f = \left| \frac{4\pi sin(\phi)}{24 \cdot 60 \cdot 60} \right| \tag{1}$$

$$\beta = \frac{e\rho(V_R^2 + fV_R R_{\mathrm{MW}})}{\Delta P} \tag{2}$$

$$V(r) = \sqrt{\frac{\frac{R_{\mathrm{MW}}}{r}^{\beta} \beta \Delta P e^{-\frac{R_{\mathrm{MW}}}{r}^{\beta}}}{\rho}} - \frac{fr}{2} \tag{3}$$

where f is the Coriolis parameter, ϕ the eye latitude, β a term capturing the steepness of the radial speed profile, V_R the maximum wind speed (at the radius of maximum winds), ρ the air density, R_{MW} the radius to maximum winds, ΔP the pressure deficit of the eye below background for the region and $V(r)$ the speed at a given radius, r.

The translational motion of the storm also produces a wind component. We approximate this with the storm eye velocity vector. This vector is reduced in magnitude by α and rotated (in the direction of cyclone rotation) by β. We take radially averaged values of $\alpha = 0.56$ and $\beta = 19.2°$ as per [30].

The translational and rotational components are vector summed, giving rise to a non-axisymmetric wind field. The degree of non-axisymmetry is a function of the ratio between the storm eye speed and V_{RMW}. Where the storm eye speed is a larger proportion V_{RMW}, there will be less axisymmetry, as in the case of weaker storms [40].

Surface wind speed

To estimate surface wind speeds we use a use a spatially varying boundary layer approximation, dependent on the local surface roughness, with a power law approach as per [26].

$$V_1 = V_2 \left(\frac{z_1}{z_2} \right)^{\frac{1}{ln(\sqrt{z_1 z_2})/R_0}} \tag{4}$$

where V_1 is the velocity at height z_1, V_2 the velocity at z_2 and R_0 the surface roughness length. We took the ESA GlobCover 2009 global land cover map [41] and converted it to surface roughness values using a modified version of the values used for the Global Wind Atlas [42].

The wind footprints have been calibrated against other model data from [32]. We chose to calibrate against model rather than observation data as it is available as complete fields, allowing for many more comparisons than against point station data. Reanalysis data, such as ERA5, which combines observation and model results, could have been used, but is not available at a sufficiently high resolution to resolve the eye of a TC where wind speed varies rapidly as a function of space.

Done et al. [32] simulated IBTrACS historic storms with a gradient-level parametric wind model and then brought these winds to the surface level with a physical boundary layer model (which is too computationally intensive to practically use for thousands of events) as derived by [43]. There were 458 storms common to our work and Done's catalogue. We treated the $\frac{z_1}{z_2}$ ratio from equation 4 as a free parameter to calibrate against Done et al. This ratio was varied until the mean error (across all pixels and speeds) was minimal (with $\frac{z_1}{z_2} = 1.8$ giving $\mu_{error} = 0.2\mathrm{ms}^{-1}$).

The post-calibration pixelwise comparison of wind speed for all storms and all pixels within 200km of the storm eye is shown as Figure 7. With the population bias removed by the calibration, lower wind speeds (10-50ms^{-1}) have median errors within 2ms^{-1} of Done et al., with p_{25} and p_{75} not exceeding 5ms^{-1} absolute error. At higher wind speeds, our model increasingly underestimates wind speeds compared to Done et al., with a median error for the 60-70ms^{-1} band of approximately -5ms^{-1} and for 70-80ms^{-1}, -7ms^{-1}. For this work, electricity outage estimates will be most sensitive to wind speed errors around our transmission line failure thresholds. These are typically in the 30-40ms^{-1} bracket, with a median error of $\approx$ 1ms^{-1} and 90% of values within $\pm$7ms^{-1}.

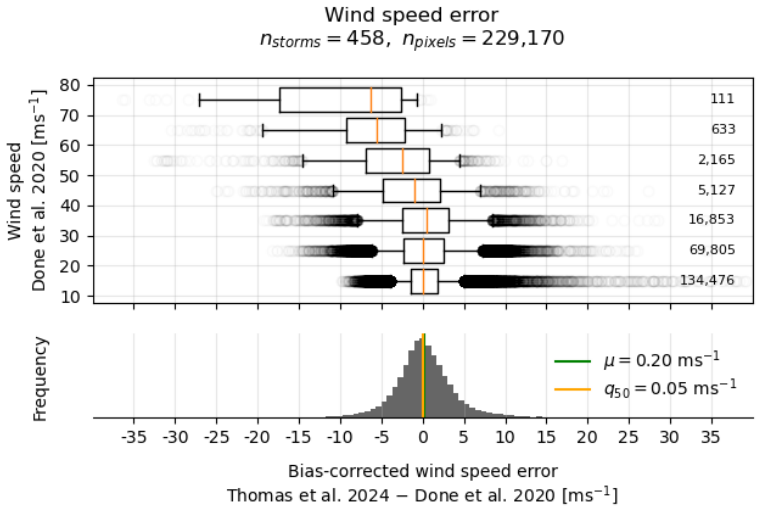

Figure 7: Post-calibration discrepancy between wind speeds generated for this work and [32]. Data drawn from 458 storms, where 229,170 pixels were within 200km of a storm eye that was over land. The lower panel shows the distribution of errors, taking Done et al. to be truth. The upper panel shows the breakdown as a function of Done et al.'s estimated wind speed. The box plots show the interquartile range and the median, with whiskers at the 5^{th} and 95^{th} percentiles and any outliers. Numbers of pixels per wind speed band are given on the right.

Calibration and validation of wind threshold of electricity asset failure

The damage threshold (v_{th}) of the outage model was determined using satellite-based nighttime light (NTL) observations from the Black Marble dataset (VNP46A2)[44], which provides global daily NTL at a spatial resolution of 15 arc second (approximately 450 meters at the equator) since January 2012. The calibration was conducted using historical storms occurred worldwide from 2012–2023, obtained from the International Best Track Archive for Climate Stewardship (IBTrACS V4[13]). A total of 315 were analyzed, with an 80/20 split for calibration and validation (i.e., 252 and 63 storms, respectively; see Figure 8). These storms impacted 44 countries (see Table 1).

The model performance with eight damage thresholds (20 to 45 m s^{-1} in 2.5 m s^{-1} increments) was evaluated by comparing the modelled outage and blackout detected from NTL, using Franks' index[45]:

$$F_{th} = 1 - \frac{|A_{mod,th} - A_{obs}|}{A_{obs}} \tag{5}$$

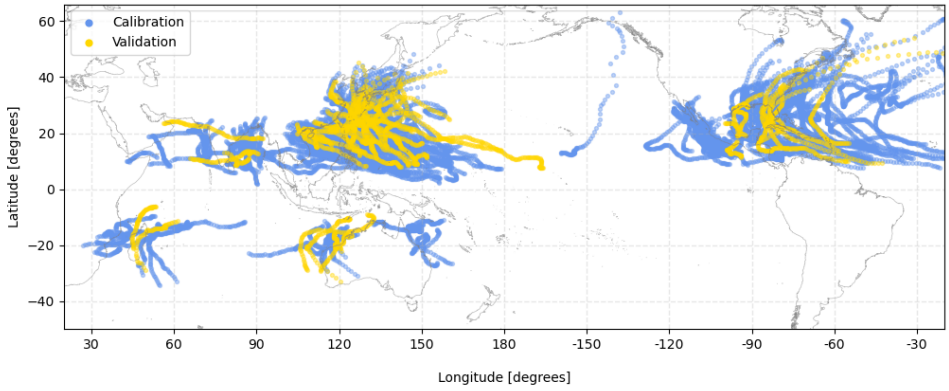

Figure 8: IBTrACS historic tracks as used for calibration and validation of wind speed damage thresholds.

whereby $A_{mod,th}$ and A_{obs} represent the number of sinks predicted as modelled and observed to be impacted, respectively. Frank's index from $-\infty$ to 1, with a value closer to 1 indicates better model performance. As illustrated in Figure 6 e), the optimal damage threshold attains the highest Frank's index as it reproduces the correct number of disconnected sinks.

A modelled outage was defined when a sink's post-storm connected power supply fell below 90% of its pre-storm level. To account for the background noise and regional variations associated with the NTL data, we computed the before-storm baseline NTL of each sink (spatial mean) over the 3 months preceding each storm. To address the issue of missing data due to cloud cover, a 10-day post-storm composite image was generated, in which each pixel was filled with the first available high-quality persistent nighttime lights within 10 days following the storm. The post-storm NTL of each sink (spatial mean) was then estimated from this composite image. An NTL blackout was identified when the post-storm NTL of a sink is significantly lower (one-tailed test at the 0.9 significance level) than its baseline. High-income counties exhibited a higher threshold compared to other counties, with optimal thresholds of 35 m s^{-1} and 30 m s^{-1}, respectively, and validation accuracies of 0.76 and 0.90 (Table S1).

Table 1: Countries passed by historical storms for model calibration, thresholds chosen for different income groups, and the associated Franks' index values based on the validation dataset (i.e., 20% of the historical storms that were not used in model calibration).

Income group		Country	v_{th}	Franks' index
High income (18 counties)		United States of America, Japan, South Korea, Hong Kong, Macau, Taiwan, Canada, Guam, Australia, Puerto Rico, Panama, Trinidad and Tobago, Norway, United Kingdom, Ireland, Oman, Portugal, Spain	35	0.76
Other	Upper middle income (11 countries)	Mexico, China, Cuba, Dominican Republic, Jamaica, Guatemala, Saint Lucia, Thailand, Costa Rica, Venezuela, Malaysia	30	0.90
	Lower middle income (11 countries)	Vietnam, Philippines, Laos, India, Bangladesh, Honduras, Nicaragua, Myanmar, Cambodia, El Salvador, Sri Lanka, Haiti		
	Low income (4 countries)	Madagascar, Mozambique, North Korea		

While the Black Marble data has been widely used in assessing electricity outages following storms (e.g.,[46][47][48][49][50][51]), it is important to recognize two major sources of uncertainty: geometric error and angular error. Geometric error arises from the spatial observational coverage mismatch of the sensor[52], and can be mitigated by averaging NTL of over an area[53][54]. In this study, we addressed this issue by computing the spatial mean of NTL for each sink. Angular error results from variation in the view angle of the satellite[55]. To account for this, we estimated the pre-storm baseline for each unit using NTL data from the three months preceding the storm. This approach helps mitigate angular error by incorporating periodic changes in the satellite's view angle and reducing other sources of noise, such as those caused by weekly and seasonal activity[52][56]. A further challenge in using daily NTL data is the large amount of missing data caused by cloud coverage[57] and is often mitigated by constructing composite impage[58]. Given the short-lived nature of power outages, we developed 10-day composites using the earliest available high-quality measurements within 10 days following the storm.

To further assess the accuracy of our in NTL blackout, we compared the blackouts detected and events registered in the PowerOutage.US (POUS[59]) records of power cuts in the US from 2017–2022, at an hourly time step. Twenty-four storms were found to cause power cuts in the US during this period. We discarded data for counties with less than 5% of the total county population were tracked. An outage event was defined when the number of customers connected is less than 90% of the customers tracked. Indeed, NTL data is more powerful in detecting longer events, with registration rate being 90% for events longer than 5 days, compared to 63% for events lasting 1-4 days (Table S2). Nevertheless, the overall registration rate for events that lasted for 1 day or longer is 60%. The bias toward longer events is likely due to the daily temporal resolution of NTL and data gaps caused by cloud coverage. In addition, the NTL data are more likely to capture

storm makes landfall in the evening, as those landfall in the morning could be restored by evening. However, we expect that our global study would help to balance out the effects of different landfall times.

Table 2: Number of events reported in POUS and registered in NTL.

Duration (days)	1-4	5-9	10-14	15-19	>=20
POUS	571	110	22	11	14
NTL	357	100	21	11	10
Registration rate	63	91	95	100	71